

Research Article

Active and Reactive Power Control for Wind Turbines Based DFIG Using LQR Controller with Optimal Gain-Scheduling

Ashraf Radaideh , Mu'men Bodoor , and Ayman Al-Quraan 

Electrical Power Engineering Department, Yarmouk University, Irbid, Jordan

Correspondence should be addressed to Ashraf Radaideh; a.radaideh@yu.edu.jo

Received 19 May 2021; Revised 24 July 2021; Accepted 15 September 2021; Published 6 October 2021

Academic Editor: François Vallée

Copyright © 2021 Ashraf Radaideh et al. This is an open access article distributed under the Creative Commons Attribution License, which permits unrestricted use, distribution, and reproduction in any medium, provided the original work is properly cited.

This paper proposes an optimal gain-scheduling for linear quadratic regulator (LQR) control framework to improve the performance of wind turbines based Doubly Fed Induction Generator (DFIG). Active and reactive power decoupling is performed using the field-oriented vector control which is used to simplify DFIG's nonlinearity and derive a compact linearized state-space model. The performance of the optimal controller represented by a linear quadratic regulator is further enhanced using the whale optimization algorithm in a multiobjective optimization environment. Adaptiveness against wind speed variation is achieved in an offline training process at a discretized wind speed domain. Lookup tables are used to store the optimal controller parameter and called upon during the online implementation. The control framework further integrates the effects of pitch angle control mechanism for active power ancillary services and possible improvements on reactive power support. The results of the proposed control framework improve the overall performance of the system compared to the conventional PI controller. Comparison is performed using the MATLAB Simulink platform.

1. Introduction

Electricity is one of the life necessities that made a quantum leap in the world. Traditionally, electrical energy is primarily produced using fossil fuel energy resources. However, nowadays, the world is witnessing high production levels from Renewable Energy Sources (RES). Wind turbines (WTs) are among the leading and fast-growing technologies over extended geographical areas. Worldwide, the total installed capacity in 2019 is 650 GW. More than 93 GW is installed in the year 2020 bringing the total installed capacity to 743 GW despite the COVID-19 pandemic. This indicates the importance and effectiveness of power production using WTs [1].

Wind turbines are initially designed and operated with fixed-speed induction machines to avoid additional costs associated with power electronic converters. However, to improve the conversion efficiency, the variable speed drive system becomes more dominant. Doubly Fed Induction Generator (DFIG) facilitates the variable speed feature

through a reduced size converter. This explains the widespread use of DFIGs with wind turbines. DFIG's stator is directly connected to the grid at the nominal grid frequency and its wound rotor through a bidirectional back-to-back voltage source converters (VSC) but at variable frequency [2, 3].

In many countries, the integration of wind turbines with the grid should follow strict codes and standards. Additional features and capabilities traditionally overlooked have become mandatory in new designs such as low voltage ride-through, frequency regulation, and reactive power support. Voltage dips result in large rotor currents due to the high voltages induced in the rotor windings. Therefore, DFIGs are very sensitive to voltage sags. Large rotor currents may destroy the Rotor Side Converter (RSC) if not appropriately disconnected by the protection devices. Hence, the wind turbine will be out of service during faulty conditions [4, 5].

1.1. Related Work. The history of DFIG development in WTS and the different representations of modeling and control techniques are provided in [5]. Modeling and

control frameworks presented in the literature are subjected to analyze and enhance the performance of DFIG in both transients and steady-state operations. Modeling practices with the corresponding control system include direct torque control [6, 7], direct power control [8–11], stator field orientation [11], and stator voltage orientation [12–15].

Vector control technique, that is, the voltage and field orientation, requires phase locked loops and advance control systems to achieve decoupling between torque, active, and reactive power. Conventional control techniques with PI regulators are usually utilized based on machine mode in the synchronous (d - q) reference frame [15–18]. On the other hand, direct control techniques, that is, torque and power, utilize a more simpler control system. However, the control techniques mandate uneven switching frequencies among the power electronic switches causing nonuniform distribution of heat and losses.

Extracting the maximum available power of variable speed WTS mandates operating at the maximum available efficiency. Control design adjustments are required to achieve this purpose. The authors in [18] suggest implementing a linearization feedback regulator for MPPT efficiency improvement. In [19], a control scheme through a feedback algorithm is proposed to adjust the power flow of the DFIG, improve the system reliability, and reduce voltage disturbances.

A model reference adaptive system observer is presented in [20]. The system provides a prediction of the rotor position estimation errors under parameters mismatch for sensorless control of a stand-alone DFIG. A model predictive stator current control scheme is investigated in [21]. Compared with the traditional vector control, the proposed method can reach a faster dynamical response.

A sliding mode control (SMC) scheme is introduced and applied in [22]. The direct power control (DPC) methodology is utilized to overcome the conventional vector control scheme difficulties. A robust sliding mode control strategy is provided [23] to overcome perturb-and-observe technique failure in the presence of sudden wind speed variations.

Adaptive control systems have become widely used and accepted in various fields and industrial applications, including power systems and wind energy conversion systems [24, 25]. The authors in [26] design an adaptive observer for stand-alone DFIG. A reduced-order observer adaptive to speed changes is proposed for grid-connected DFIG in [27]. An adaptive neurofuzzy system is implemented in [28] for distributed DFIG systems. An adaptive maximum power tracking system to control the rotor speed of DFIG is proposed in [29]. The work in [30] introduces an adaptive second-order sliding mode control with a receding horizon control system for DFIG. The authors in [31] designed an adaptive fractional-order sliding mode control for the DFIG system. A new adaptive direct power control strategy is investigated in [32], where the constant switching table is replaced by an adaptive technique updated online according to the reactive power changes and the previous switching sequence.

Optimal design of PI controller for variable speed wind turbine based grey wolf optimizer is presented in [33].

Compared with different heuristic algorithms, the proposed method shows better tracking to the Maximum Power Point (MPP). The work provided in [34] shows a cascaded nonlinear regulator design based on fuzzy logic concept for optimal power tracking. Moreover, stator real and reactive power regulation is accomplished using 2nd-order sliding mode controller. Robust neuronal controller design is presented in [35] to overcome the conventional PI controller difficulties through parameters variation.

To overcome drawbacks of PI control mechanism manifested in difficult dynamic analysis for multiple-input and multiple-output systems and poor performance at parameter variations, an optimal controller is utilized with LQR in [36, 37] and with multivariable H_{∞} controller in [38]. The authors in [39] present a new control strategy of the DFIG based wind turbine operating at one wind speed using the linear quadratic regulator (LQR) with optimal weighting matrices chosen based on Genetic Algorithm. The main objective is to improve the dynamic response, reliability, and stability of the system.

Reactive power ability of wind turbine based DFIG is introduced in [40]. The study provides the limitations on DFIG's reactive power support or consumption based on the stator and rotor currents and the rated value of rotor voltage. A new low voltage ride-through strategy for reactive power support is proposed in [41]. The study suggests that, during faults, part of the energy captured from the wind is stored in the rotor's inertia.

This paper proposes a multiple-input and multiple-output linear quadratic regulator with gain-scheduling for wind turbine system based DFIG. Frequency- and time-domain system responses such as settling time, peak time, percent overshoot, steady-state error, and damping are gathered to form a multiobjective function. The objective function is implemented with the whale optimization algorithm to select the optimal weighting matrices at various wind speeds during offline process. The results are stored in lookup tables which are used during the online implementation. The performance of the LQR with optimal gain-scheduling is compared with the conventional PI controller. In addition, pitch angle control is augmented to the controller design enabling active power curtailments while improving the reactive power supporting capability.

1.2. Contributions. The main contributions added to the literature can be summarized as follows:

- (1) A linear quadratic regulator with optimal gain-scheduling control architecture is proposed. The controller preserves linearity, compactness, and robustness against wind speed variations. This improves both the performance and the net energy yield from wind turbines.
- (2) Effects of pitch angle control are augmented to the model and the controller for real power curtailments and its possible consequences on the reactive power support.

- (3) The performance of the controller is enhanced in a multiobjective optimization platform. The objective function combines system stability, oscillations, and time-domain specifications.

1.3. Paper Outline. The outline of the paper is demonstrated as follows. Initially, the principle of operation of wind turbines and related mathematical models are presented in Section 2. In Section 3, DFIG's detailed mathematical model is derived including the grid-side converter and the DC link. Machine's linearization under vector control environment and the state-space representation are discussed in Section 4. Section 5 presents the conventional PI controller as well as the proposed optimal gain-scheduling control framework. Limitations on wind turbine reactive power capability are discussed in Section 6. In addition, the effect of pitch angle control is presented. Simulation results are illustrated in Section 7. Finally, the paper is concluded in Section 8.

2. Wind Turbine Aerodynamics

The operation of wind turbines is based on extracting wind's kinetic energy and converting the captured energy into electrical energy using generators. The behavior is governed by the momentum theory where the kinetic energy existing in the mainstream wind is expressed as shown in (1). Only a fraction of wind power can be extracted based on the energy conversion efficiency. The power coefficient C_p shown in (1) reflects the efficiency of conversion from wind energy to mechanical energy and is usually expressed as a function of the tip speed ratio (λ) shown in (2) which defines the ratio between the linear speed at the blade's tip and the wind speed [4, 5].

$$P_w(v) = \frac{1}{2} \rho A_t v^3, \quad (1)$$

$$P_t(v) = \frac{1}{2} \rho \pi R^2 v^3 C_p,$$

$$\lambda = \frac{R\Omega_t}{v}. \quad (2)$$

The torque developed in wind turbines (3) can be expressed using the captured power and the rotational speed of the turbine. The torque coefficient (C_t) is defined as the power coefficient over the tip speed ratio [2].

$$T_t = \frac{\rho \pi R^2 v^3 C_p}{2\Omega_t} = \frac{\rho \pi R^3 v^2 C_p}{2\lambda} = \frac{1}{2} \rho \pi R^3 v^2 C_t, \quad (3)$$

$$C_t = \frac{C_p}{\lambda}. \quad (4)$$

The power coefficient has a maximum theoretical value called the Betz limit which equals 0.593 for wind turbines. Power coefficient is given by the manufacture as a function of the tip speed ratio and the pitch angle β . A common practice is to express the power coefficient analytically in an

exponential model as shown in (5) and (6). Parameter (λ_i) is a time-varying parameter because of the changing nature of the tip speed ratio (λ) [4].

$$C_p = k_1 \left\{ \frac{k_2}{\lambda_i} - k_3 \beta - k_4 \beta^{k_5} - k_6 \right\} e^{-k_7/\lambda_i}, \quad (5)$$

$$\lambda_i = \frac{1}{(1/\lambda + k_8 \beta) + (k_9/\beta^3 + 1)}. \quad (6)$$

3. Mathematical Models

The typical configuration of grid-connected DFIG is shown in Figure 1; the stator is supplying constant voltage amplitudes and frequency to the grid. The rotor is connected with a three-phase back-to-back converter which can be controlled to provide three-phase voltages with different amplitudes and frequencies. This feature helps achieve different operating conditions while controlling the rotational speed of the rotor. As a result, the operation can be controlled to extract the maximum power. This feature does not exist in the fixed-speed configuration.

3.1. DFIG Model. The dynamic ($d-q$) (synchronous) rotating reference frame is the most commonly used coordinate to represent the mathematical model of the DFIG machine. After applying the required rotational transformations, relationships governing the stator voltage (v_{ds}, v_{qs}), rotor voltage (v_{dr}, v_{qr}), stator magnetic flux (Ψ_{ds}, Ψ_{qs}), and rotor magnetic flux (Ψ_{dr}, Ψ_{qr}) can be expressed as shown in (7)–(14) [2, 3], where $L_s = L_m + L_{\sigma s}$ and $L_r = L_m + L_{\sigma r}$.

$$v_{ds} = R_s i_{ds} + \frac{d\Psi_{ds}}{dt} - \omega_s \Psi_{qs}, \quad (7)$$

$$v_{qs} = R_s i_{qs} + \frac{d\Psi_{qs}}{dt} + \omega_s \Psi_{ds}, \quad (8)$$

$$v_{dr} = R_r i_{dr} + \frac{d\Psi_{dr}}{dt} - \omega_r \Psi_{qr}, \quad (9)$$

$$v_{qr} = R_r i_{qr} + \frac{d\Psi_{qr}}{dt} + \omega_r \Psi_{dr}, \quad (10)$$

$$\Psi_{ds} = L_s i_{ds} + L_m i_{dr}, \quad (11)$$

$$\Psi_{qs} = L_s i_{qs} + L_m i_{qr}, \quad (12)$$

$$\Psi_{dr} = L_m i_{ds} + L_r i_{dr}, \quad (13)$$

$$\Psi_{qr} = L_m i_{qs} + L_r i_{qr}. \quad (14)$$

The time derivative of stator and rotor currents can be extracted by rearranging the previous model as demonstrated in equations (15)–(18), where $\sigma = 1 - L_m^2/L_r L_s$.

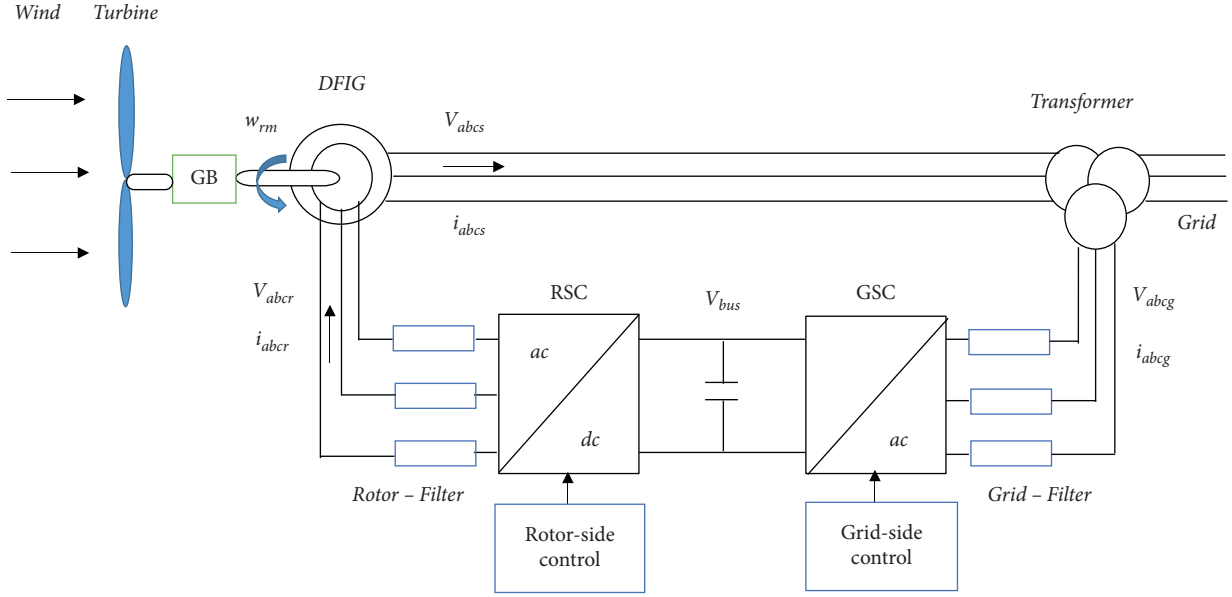


FIGURE 1: Typical configuration of grid-connected wind turbine based DFIG.

$$\frac{d}{dt}i_{ds} = \frac{1}{\sigma L_s} \left\{ v_{ds} - R_s i_{ds} - \frac{L_m}{L_r} v_{dr} + \frac{L_m R_r}{L_r} i_{dr} + \left(\omega_s L_s - \frac{L_m^2 \omega_r}{L_r} \right) i_{qs} + (\omega_s - \omega_r) L_m i_{qr} \right\}, \quad (15)$$

$$\frac{d}{dt}i_{qs} = \frac{1}{\sigma L_s} \left\{ v_{qs} - R_s i_{qs} - \frac{L_m}{L_r} v_{qr} + \frac{L_m R_r}{L_r} i_{qr} + \left(\frac{L_m^2 \omega_r}{L_r} - \omega_s L_s \right) i_{ds} + (\omega_r - \omega_s) L_m i_{dr} \right\}, \quad (16)$$

$$\frac{d}{dt}i_{dr} = \frac{1}{\sigma L_r} \left\{ v_{dr} - R_r i_{dr} - \frac{L_m}{L_s} v_{ds} + \frac{L_m R_s}{L_s} i_{ds} + \left(\omega_r L_r - \frac{L_m^2 \omega_s}{L_s} \right) i_{qr} + (\omega_r - \omega_s) L_m i_{qs} \right\}, \quad (17)$$

$$\frac{d}{dt}i_{qr} = \frac{1}{\sigma L_r} \left\{ v_{qr} - R_r i_{qr} - \frac{L_m}{L_s} v_{qs} + \frac{L_m R_s}{L_s} i_{qs} + \left(\frac{L_m^2 \omega_s}{L_s} - \omega_r L_r \right) i_{dr} + (\omega_s - \omega_r) L_m i_{ds} \right\}. \quad (18)$$

Evaluating voltages and currents in the synchronous reference frame enables calculating the active and reactive power for both the stator and the rotor (19)–(22). Also, the electromagnetic torque in d – q reference frame can be evaluated as shown in (23) [2].

$$P_s = \frac{3}{2} [v_{ds} i_{ds} + v_{qs} i_{qs}], \quad (19)$$

$$P_r = \frac{3}{2} [v_{dr} i_{dr} + v_{qr} i_{qr}], \quad (20)$$

$$Q_s = \frac{3}{2} [v_{qs} i_{ds} - v_{ds} i_{qs}], \quad (21)$$

$$Q_r = \frac{3}{2} [v_{qr} i_{dr} - v_{dr} i_{qr}], \quad (22)$$

$$T_{em} = \frac{3PL_m}{4L_s} [\psi_{qs} i_{dr} - \psi_{ds} i_{qr}]. \quad (23)$$

3.2. Modeling of Grid-Side System. The grid-side system consists of grid-side converter (GSC), filter, and grid voltages as illustrated in Figure 2. Under steady-state conditions, grid voltages (v_{ag}, v_{bg}, v_{cg}) are constant in amplitude and frequency. Meanwhile the output voltages (v_{af}, v_{bf}, v_{cf}) can be modified to achieve different voltage amplitudes and frequencies. The simplest configuration of the grid filter can be used in this analysis, which consists of a pure inductive filter (L_f) with a parasitic resistance (R_f). Electrical relationships can be derived from Figure 2 and, after applying transformation, the $(d-q)$ components of GSC voltages can be expressed as shown in (24) and (25). Therefore, the grid active and reactive power in $d-q$ reference frame can be derived as illustrated in (26) and (27), respectively [4].

$$v_{df} = R_f i_{dg} + L_f \frac{di_{dg}}{dt} + v_{dg} - \omega_s L_f i_{qg}, \quad (24)$$

$$v_{qf} = R_f i_{qg} + L_f \frac{di_{qg}}{dt} + v_{qg} + \omega_s L_f i_{dg}, \quad (25)$$

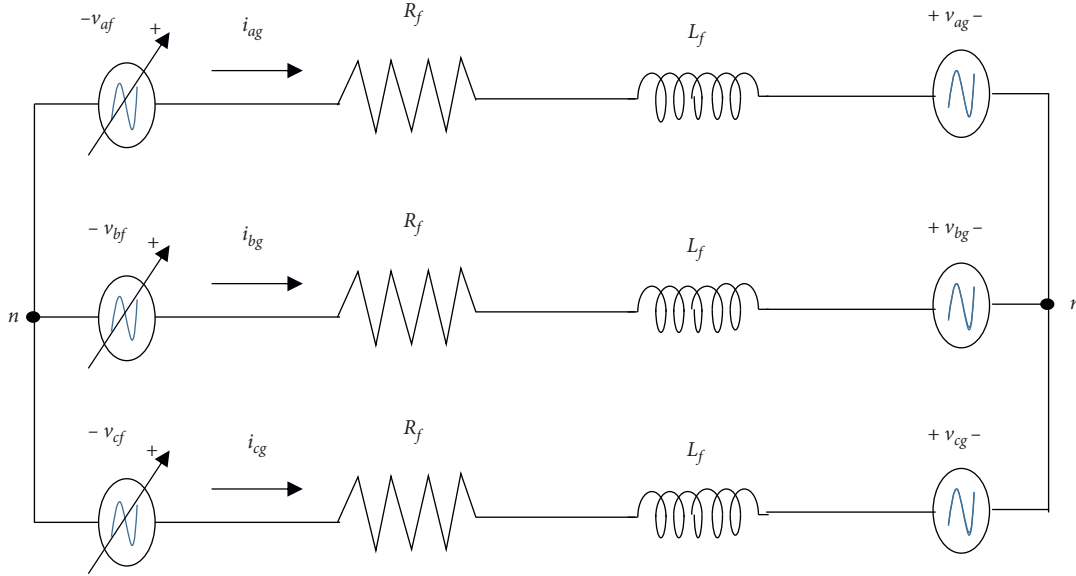


FIGURE 2: Three-phase grid-side system representation.

$$P_g = \frac{3}{2} [v_{dg}i_{dg} + v_{qg}i_{qg}], \quad (26)$$

$$Q_g = \frac{3}{2} [v_{qg}i_{dg} - v_{dg}i_{qg}]. \quad (27)$$

3.3. Wind Turbine Modeling. The swing equation (28) captures the relationship that governs the mechanical shaft operation. Our main attention is focused on the region of Maximum Power Point Tracking (MPPT) (demonstrated in the power-speed curve shown in Figure 3 as region 2). In this region, the objective is to follow the maximum power extraction curve where the wind speed is below the rated value. Different strategies are proposed to control the wind turbine to track the curve of the Maximum Power Point. In this work, an indirect speed controller is used to regulate the electromagnetic torque which mathematically appears as a quadratic function of the turbine speed (Ω_t). In this context, the pitch angle is kept at the optimum value. Following the previous argument, wind turbines operating at the zone of MPPT have the coefficients illustrated in (29) [4].

$$J \frac{dw_{rm}}{dt} = T_{em} + T_{mech}, \quad (28)$$

$$\begin{aligned} \lambda_{opt} &= \frac{R\Omega_t}{V}, \\ C_p &= C_{p,max}, \\ \beta &= \beta_{opt}. \end{aligned} \quad (29)$$

The relationship between the DFIG electromagnetic torque and the turbine torque can be demonstrated as shown in (30)–(32). D_t and D_m are the damping coefficients for both the turbine and the machine and N represents the gearbox ratio. A more simplified but less accurate model can be obtained if both damping coefficients are neglected [4].

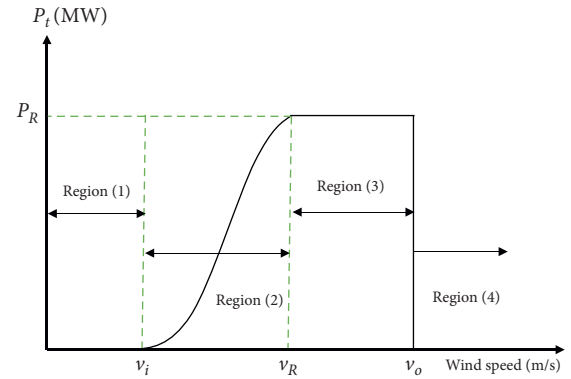


FIGURE 3: Power-speed curve of wind turbines.

$$T_{em} = -\frac{T_t}{N} + (D_t + D_m)w_{rm} \quad (30)$$

$$= -k_{opt}w_{rm}^2 + (D_t + D_m)w_{rm},$$

$$k_{opt} = \frac{1}{2} \rho \pi \frac{R^5}{\lambda_{opt}^3 N^3} C_{p,max}, \quad (31)$$

$$w_{rm} = N\Omega_t. \quad (32)$$

3.4. Modeling of DC Link. The DC link capacitor acts as an energy storage device that is installed between the RSC and GSC with a capacitance of C_{bus} . It works as a source of reactive power which provides the magnetizing current at the rotor. By assuming that the converter losses are ignored, the DC bus power (P_{dc}) can be estimated as the difference between rotor and grid active power. In order to monitor the DC bus voltage, the DC link power can be alternatively expressed as shown in the following equation [39]:

$$P_{dc} = P_r - P_g = v_{dc}i_{dc} = v_{dc}C_{bus}\frac{dv_{dc}}{dt}. \quad (33)$$

4. Vector Control Orientation

The main principle of vector control orientation is to align machine flux and grid voltage space vectors with one of the two synchronously rotating ($d-q$) reference frames. In this study, the orientation is implemented on the d -axis to achieve a decoupled control for both the active and reactive power of the stator and the grid.

4.1. Rotor-Side Converter Vector Control. The vector control technique is applied to the DFIG model represented in the synchronously rotating ($d-q$) reference frame. This method assumes that the d -axis is forced to align with the stator flux space vector. Accordingly, the stator flux is attributed to only the d -axis component, while the q -axis component is forced to zero as shown in (34). Following this assumption and substituting flux linkage equations in rotor voltage equations, we have the rotor voltages as a function of the rotor current and stator flux as demonstrated in (35) and (36) [2].

$$\Psi_{ds} = |\vec{\Psi}_s|, \quad (34)$$

$$\Psi_{qs} = 0,$$

$$v_{dr} = R_r i_{dr} + \sigma L_r \frac{d}{dt} i_{dr} - \omega_r \sigma L_r i_{qr} + \frac{L_m}{L_s} \frac{d}{dt} |\vec{\Psi}_s|, \quad (35)$$

$$v_{qr} = R_r i_{qr} + \sigma L_r \frac{d}{dt} i_{qr} + \omega_r \sigma L_r i_{dr} + \omega_r \frac{L_m}{L_s} |\vec{\Psi}_s|, \quad (36)$$

and, under steady-state conditions, the stator voltage is constant. Accordingly, the stator flux is also constant, and its rate of change is zero. Therefore, the term $d/dt|\vec{\Psi}_s|$ in equation (35) is neglected. Moreover, the voltage drop component across the stator resistance in the relation ($\vec{V}_s = \vec{I}_s R_s + j\omega_s \vec{\Psi}_s$) has a relatively small magnitude and hence can be ignored. Therefore, both of stator voltage and stator flux are perpendicular and the stator ($d-q$) voltages are simplified as shown in the following equation:

$$\begin{aligned} v_{qs} &= |\vec{v}_s|, \\ v_{ds} &= 0. \end{aligned} \quad (37)$$

Following the previous discussion, the stator real and reactive power previously expressed in (19) and (21) can be reformulated as shown in (38). Also, the electromagnetic torque formula in $d-q$ reference frame expressed in (23) can be rearranged by utilizing the alignment of the stator flux with the d -axis as demonstrated in (39) [2].

$$P_s = \frac{3}{2} [v_{qs} i_{qs}], \quad (38)$$

$$Q_s = \frac{3}{2} [v_{qs} i_{ds}],$$

$$T_{em} = -\frac{3P}{4} \frac{L_m}{L_s} \psi_{ds} i_{qr}. \quad (39)$$

4.2. Grid-Side Converter Vector Control. Further simplifications can be obtained for the grid-side converter by forcing the d -axis of the rotating reference to align with the grid voltage space vector (\vec{V}_g). Following this orientation, the q -axis component of grid voltage will be zero as shown in (40). Both grid-side voltages can be simplified as shown in (41) and (42). Further, both of grid real and reactive power equations are reformulated as demonstrated in (43) [4].

$$v_{dg} = |\vec{v}_g|, \quad (40)$$

$$v_{qg} = 0,$$

$$v_{df} = R_f i_{dg} + L_f \frac{di_{dg}}{dt} + v_{dg} - \omega_s L_f i_{qg}, \quad (41)$$

$$v_{qf} = R_f i_{qg} + L_f \frac{di_{qg}}{dt} + \omega_s L_f i_{dg}, \quad (42)$$

$$P_g = \frac{3}{2} [v_{dg} i_{dg}], \quad (43)$$

$$Q_g = -\frac{3}{2} [v_{dg} i_{qg}].$$

4.3. State-Space Representation. The entire system of the grid-connected wind turbine based DFIG can be characterized by a set of nonlinear ordinary differential equations as shown in (44)–(49). The equations are derived by rearranging the relations obtained previously for the DFIG machine, the grid-side filter, the wind turbine mechanical model, and the DC link. The entire model can be linearized around any particular steady-state operating point and then used to derive an appropriate state-space model. After linearization, all state-space matrices become linear, which are expressed as (A, B, C, D) as shown in (50) and (51) [39]. The first-order approximation of Taylor Series expansion is used to serve this purpose.

$$\frac{d}{dt} i_{dr} = \frac{1}{\sigma L_r} \left(v_{dr} - R_r i_{dr} + \left(\omega_s - \frac{p}{2} \omega_{rm} \right) \sigma L_r i_{qr} \right), \quad (44)$$

$$\begin{aligned} \frac{d}{dt} i_{qr} &= \frac{1}{\sigma L_r} \left(v_{qr} - R_r i_{qr} - \left(\omega_s - \frac{p}{2} \omega_{rm} \right) \sigma L_r i_{dr} \right) \\ &\quad - \frac{1}{\sigma L_r} \left(\omega_s - \frac{p}{2} \omega_{rm} \right) \frac{L_m}{L_s} \Psi_{ds}, \end{aligned} \quad (45)$$

$$\frac{d}{dt}i_{dg} = \frac{1}{L_f}(v_{df} - R_f i_{dg} - v_{dg} + \omega_s L_f i_{qg}), \quad (46)$$

$$\frac{d}{dt}i_{qg} = \frac{1}{L_f}(v_{qf} - R_f i_{qg} - \omega_s L_f i_{dg}), \quad (47)$$

$$\frac{d}{dt}w_{rm} = -\frac{3P}{4J} \frac{L_m \Psi_{ds}}{L_s} i_{qr} + \frac{k_{opt} w_{rm}^2}{J}, \quad (48)$$

$$\frac{d}{dt}v_{dc} = \frac{3}{2C_{dc} v_{dc}} (v_{dr} i_{dr} + v_{qr} i_{qr} - v_{df} i_{dg} - v_{qf} i_{qg}), \quad (49)$$

$$\delta \dot{\mathbf{x}} = \mathbf{A} \delta \mathbf{x} + \mathbf{B} \delta \mathbf{u}, \quad (50)$$

$$\delta \mathbf{y} = \mathbf{C} \delta \mathbf{x} + \mathbf{D} \delta \mathbf{u}, \quad (51)$$

where $w_r = \omega_s - p/2w_{rm}$, \mathbf{x} is the state variable vector, \mathbf{u} is the input variable vector, \mathbf{y} is the system output, and \mathbf{A} , \mathbf{B} , \mathbf{C} , and \mathbf{D} are the dynamics or state matrix, the input matrix, the output or sensor matrix, and the feed-through matrix, respectively. The deviations in state variables, input variables, and output variables are defined as shown in (52), (53), and (54), respectively. The system output is assumed to be the same as the state vector (\mathbf{x}). Therefore, matrix \mathbf{C} is a (6×6) identity matrix. However, since there is no direct relation between the input and the system output, matrix \mathbf{D} is a (6×4) zero matrix.

$$\delta \mathbf{x} = [\delta i_{dr} \delta i_{qr} \delta i_{dg} \delta i_{qg} \delta w_{rm} \delta v_{dc}]^T, \quad (52)$$

$$\delta \mathbf{u} = [\delta v_{dr} \delta v_{qr} \delta v_{df} \delta v_{qf}]^T, \quad (53)$$

$$\delta \mathbf{y} = [\delta i_{dr} \delta i_{qr} \delta i_{dg} \delta i_{qg} \delta w_{rm} \delta v_{dc}]^T. \quad (54)$$

Determining the current steady-state operation point requires prior knowledge of the mainstream wind speed and the operating power factor (stator reactive power Q_s and GSC reactive power Q_g). Following the steps illustrated in Algorithm 1, the current operating point can be easily evaluated and further automated. The time derivatives of all state variables in equations (44)–(49) are set to zero at steady state.

5. Control Techniques

This section discusses the control aspects based on the conventional PI controllers, conventional LQR controller, and the optimal gain-scheduling LQR control schemes.

5.1. PI Controller. The control system based on PI regulator is described in different stages. First, it is required to establish the current control loops for both the RSC and GSC. Second, the outer power and speed control loops can be constructed. The last stage requires tuning appropriate gains

for the controllers. Because of the alignment made with the stator flux space vector, rotor current components can provide the ability to independently control stator real and reactive power as demonstrated in (55) and (56). It is clearly shown that the machine power and torque are proportional to the rotor quadrature current component. Therefore, by adjusting (i_{qr}), it is possible to regulate the machine's torque, speed, and real power. On the other hand, stator reactive power regulation can be achieved by controlling the rotor direct current component (i_{dr}) [2].

$$P_s = -\frac{3}{2} \frac{L_m}{L_s} i_{qr} v_{qs} = K_P i_{qr}, \quad (55)$$

$$Q_s = K_Q \left(i_{dr} - \frac{\Psi_{ds}}{L_m} \right), \quad (56)$$

$$K_P = K_Q = -\frac{3}{2} \omega_s \frac{L_m}{L_s} \Psi_{ds}. \quad (57)$$

The RSC control system is responsible for producing appropriate rotor voltages to attain the desired stator's real and reactive power. Therefore, two main control loops are required. First, inner rotor currents loops were described previously in (35) and (36), where the rotor voltages are functions of the rotor currents and stator flux. Second, outer power and speed loops were illustrated in equations (55) and (56). In addition, the voltage source GSC controls the DC link voltage and the reactive power transfer between the turbine and the network. Regulating the DC link voltage is essential to prevent capacitor drainage in both the hyper-synchronous and the subsynchronous modes of operation, where the power flow direction between the rotor and the grid is different. The active power transfer through the converter is indirectly controlled through V_{bus} controller. The complete control block diagram using PI controllers is demonstrated in Figure 4.

For simplicity, cross-terms that appeared in control loops for both voltage source converters can be ignored. As a result, an equivalent second-order closed-loop system can be derived as shown in (58) and (59). Following the same procedure, the reactive power equivalent closed-loop system reassembles a first-order system as shown in (60) [3].

$$\frac{i_{(d,q)r}}{i_{(d,q)r}^*} = \frac{sk_{p(2,3)} + k_{i(2,3)}}{\sigma L_r s^2 + (k_{p(2,3)} + R_r) + k_i}, \quad (58)$$

$$\frac{i_{(d,q)g}}{i_{(d,q)g}^*} = \frac{sk_{p(5,6)} + k_{i(5,6)}}{L_f s^2 + (k_{p(5,6)} + R_f) + k_i}, \quad (59)$$

$$\frac{Q_s}{Q_s^*} = \frac{sk_{p1} + k_{i1}}{(k_{p1} + 1)s + k_{i1}}. \quad (60)$$

Pole placement of classical control theory can be utilized to locate the poles at desired locations. The characteristic equation of the new locations mandates a specific damping ratio and natural frequency. In this study, the damping ratio (ζ) is selected as one for critically damped responses.

```

(1) procedure
(2) Define  $v \leftarrow$  Wind speed
(3) Define  $Q_s \leftarrow$  Stator reactive power
(4) Define  $Q_g \leftarrow$  GSC reactive power
(5) calculate  $\neq$ :
(6)  $w_{rmo} = \lambda_{opt} * v * N/R$ 
(7)  $w_{ro} = w_s - ((p/2) * w_{rmo})$ 
(8)  $i_{qro} = (4 * K_{opt} * L_s * w_{rmo}^2) / (3 * p * \psi_{ds} * L_m)$ 
(9)  $i_{dro} = (-Q_s / (1.5 * w_s * \psi_{ds} * L_m / L_s)) + (\psi_{ds} / L_m)$ 
(10)  $i_{qgo} = -2 * Q_g / (3 * v_{qs} * \text{sqrt}(2/3))$ 
(11)  $v_{dro} = R_r * i_{dro} - (w_{ro} * \sigma * L_r * i_{qro})$ 
(12)  $v_{qro} = R_r * i_{qro} + w_{ro} * \sigma * L_r * i_{dro} + w_{ro} * L_m * \psi_{ds} / L_s$ 
(13) if  $v > v_i$  &  $v \leq v_{syn} \leftarrow$  Sub - synchronous mode then
(14) solve to find  $i_{dgo}$ , (Positive)
(15)  $R_f * i_{dgo}^2 - v_{qs} * \text{sqrt}(2/3) * i_{dgo} + R_f * i_{qgo}^2 + (v_{dro} * i_{dro} + v_{qro} * i_{qro}) = 0$ 
(16) end if
(17) if  $v > v_{syn}$  &  $v \leq v_R \leftarrow$  Hyper - synchronous mode then
(18) Solve to find  $i_{dgo}$ , (Negative)
(19)  $R_f * i_{dgo}^2 + v_{qs} * \text{sqrt}(2/3) * i_{dgo} + R_f * i_{qgo}^2 - (v_{dro} * i_{dro} + v_{qro} * i_{qro}) = 0$ 
(20) end if
(21) Finally,
(22)  $v_{dfo} = R_f * i_{dgo} + v_{qs} * \text{sqrt}(2/3) + w_s * L_f * i_{qgo}$ 
(23)  $v_{qfo} = R_f * i_{qgo} + w_s * L_f * i_{dgo}$ 
(24) end procedure
    
```

ALGORITHM 1: Operating point detection for MPPT region.

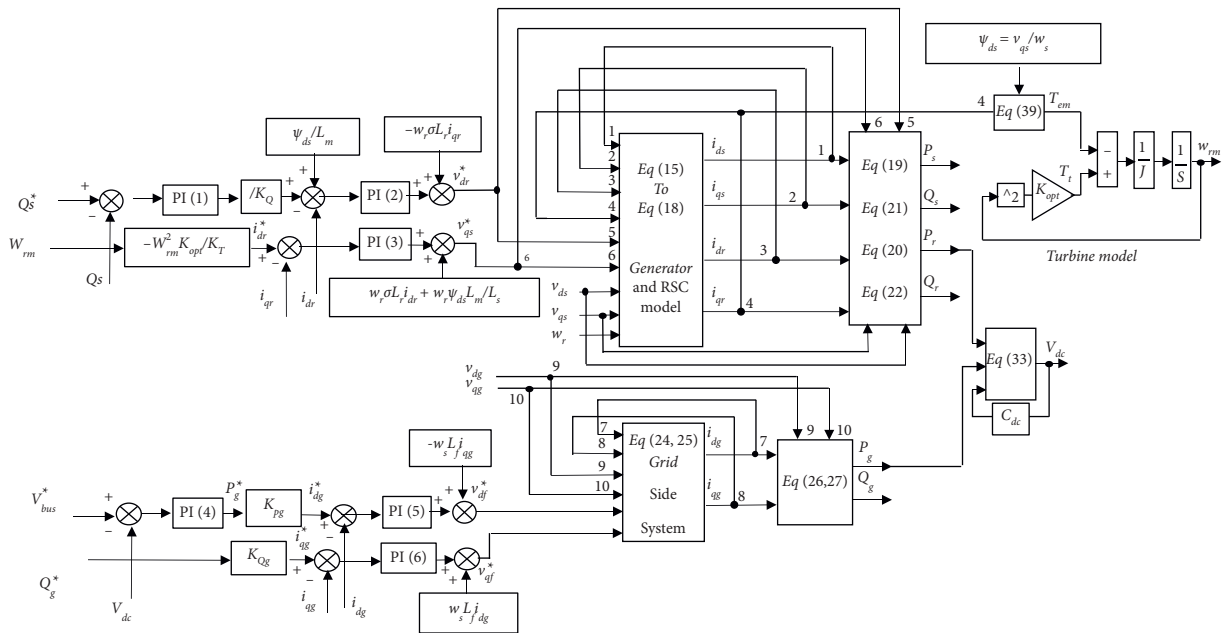


FIGURE 4: Block diagram of the simulated model with PI controller.

Therefore, the time constants for both the RSC and GSC current control loops can be found in (61). For stable operation, the inner RSC loop is selected 100 times faster than the outer one [4].

$$\tau_r = \frac{\sigma L_r}{R_r},$$

$$\tau_g = \frac{L_f}{R_f},$$
(61)

$$w_{nr} = \frac{100}{\tau_r},$$

$$w_{ng} = 2\pi f.$$
(62)

5.2. Optimized LQR Controller. LQR offers a systematic approach to obtain an optimal feedback gain able to steer a linear dynamical system to stability at minimum quadratic cost. The cost is referred to as a performance index as shown in (63). The feedback gain matrix K_{lqr} is found analytically for multiple-input multiple-output (MIMO) systems.

$$J_{LQR} = \int_0^{\infty} (\delta \mathbf{x}^T \mathbf{Q}_{lqr} \delta \mathbf{x} + \delta \mathbf{u}^T \mathbf{R}_{lqr} \delta \mathbf{u}) dt, \quad (63)$$

where \mathbf{Q}_{lqr} and \mathbf{R}_{lqr} are weighting matrices and they are characterized as semipositive and positive definite matrices. Matrix \mathbf{Q}_{lqr} guarantees appropriate convergence rates with minimum deviation errors, while \mathbf{R}_{lqr} penalizes energy expenditure on the input control signal. After evaluating \mathbf{K}_{lqr} , the optimal control efforts are found as shown in the following equation:

$$\delta \mathbf{u} = -\mathbf{K}_{lqr} \delta \mathbf{x}. \quad (64)$$

Initially, appropriate weighting matrices are chosen to achieve the best performance index. Afterward, the Riccati equation shown in (65) is solved for the positive definite matrix (\mathbf{P}_{lqr}). Finally, the optimal feedback gain matrix (\mathbf{K}_{lqr}) that maintains stability is found as shown in (66). The complete control diagram using LQR is presented in Figure 5 [39].

$$\mathbf{A}^T \mathbf{P}_{lqr} + \mathbf{P}_{lqr} \mathbf{A} - \mathbf{P}_{lqr} \mathbf{B} \mathbf{R}_{lqr}^{-1} \mathbf{B}^T \mathbf{P}_{lqr} + \mathbf{Q}_{lqr} = 0, \quad (65)$$

$$\mathbf{K}_{lqr} = \mathbf{R}_{lqr}^{-1} \mathbf{B}^T \mathbf{P}_{lqr}. \quad (66)$$

The weighting matrices \mathbf{Q}_{lqr} and \mathbf{R}_{lqr} can be chosen as identity matrices as in conventional LQR. However, this will not guarantee the best time-domain performance for the entire system. Some states or control inputs have more dominant effects compared to others. Traditionally, weighting matrices are obtained using trial-and-error procedures which are time-consuming and do not guarantee the best time-domain performance [42]. Alternatively, a more systematic approach can be used by

applying optimization techniques. In this work, whale optimization algorithm (WOA) is utilized to serve this purpose. The process is performed offline at discrete wind speed domain and then stored in lookup tables for the online implementation.

5.3. Whale Optimization Algorithm. Metaheuristic optimization algorithms are widely used by engineers, developers, and researchers for various types of optimization problems. Benchmark algorithms can efficiently find the best candidate for the global optimal solution by mimicking the evolution of a physical phenomenon existing in nature or practiced by animals' herds in hunting and mating. Whale optimization algorithm (WOA) is a population-based optimization technique inspired by the humpback whales hunting strategy. This special hunting method is known as the bubble-net feeding method. It is observed that the whales produce distinctive bubbles that can be formed as a circle or "9" shaped path. This technique is used in the exploitation and exploration strategies to find the optimal solution. Performance comparison with other benchmark metaheuristic algorithms can be found in [43].

5.4. Multiobjective Optimization. Various frequency and time-domain specifications can be considered to provide the optimum weighting matrices (\mathbf{Q}_{lqr} and \mathbf{R}_{lqr}). Based on the engineering design, some indices may have higher importance than others. In this work, the well-known stability and time-domain features will be augmented in a multiobjective optimization environment with uniformly distributed weights as demonstrated in (67). The considered performance indices of the closed-loop system ($\mathbf{A} - \mathbf{B}\mathbf{K}_{lqr}$) are the settling time (T_s), the rising time (T_r), a stability index (S_I), the peak value (P_v), the steady-state error (E_{ss}), and the system damping (D_p).

$$f_{obj} = w_1 T_s + w_2 T_r + w_3 S_I + w_4 P_v + w_5 E_{ss} + w_6 D_p, \quad (67)$$

$$\sum w_i = 1. \quad (68)$$

For the new closed-loop system matrix ($\mathbf{A} - \mathbf{B}\mathbf{K}_{lqr}$), the settling time, rising time, and peak value can be readily obtained in MATLAB for all possible combinations between the outputs and inputs. Afterward, the sum of all combinations is returned to the objective function. The steady-state error (E_{ss}) is evaluated using the expression shown in (69). The stability index (S_I) reflects how far the poles' real part is away from the complex imaginary axis, where λ_p are the system eigenvalues. The system becomes more stable with less stability index. Finally, the system damping index shown in (71) reflects the number of oscillations in the system response. Damping can be quantified by dividing the pole's imaginary parts over the poles' real parts. Thus,

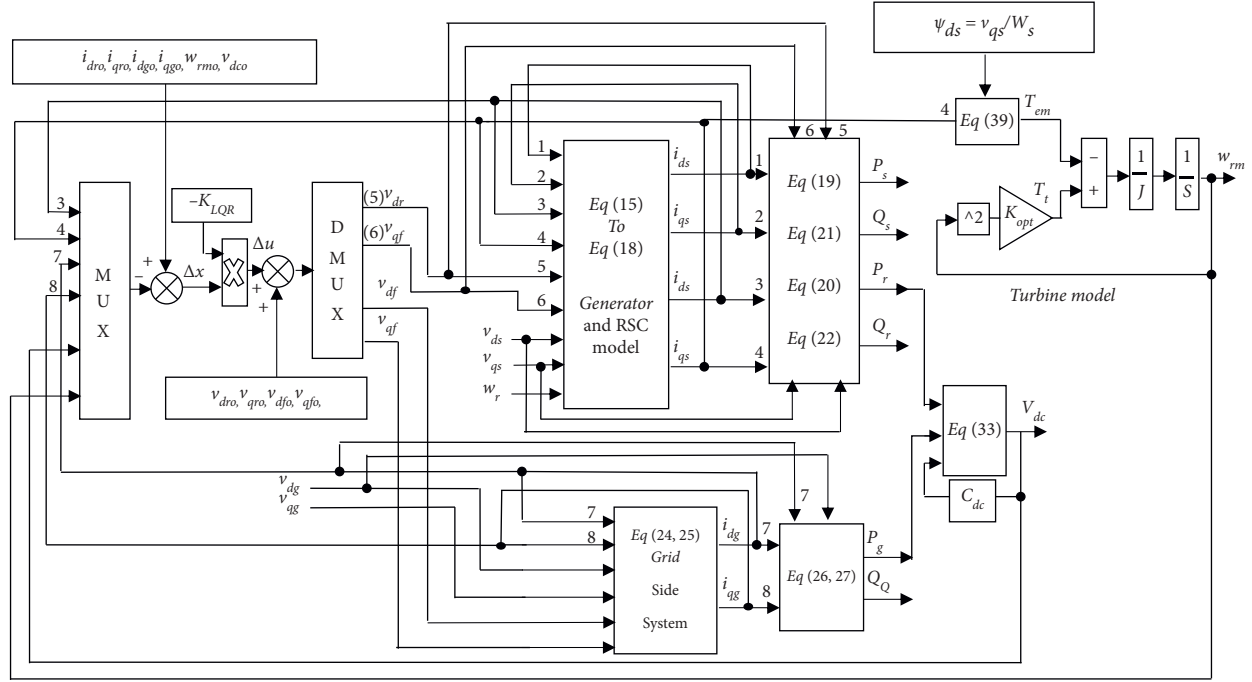


FIGURE 5: Block diagram of the simulated model with LQR controller.

damping is minimized by reducing the imaginary component of the eigenvalues.

$$E_{ss} = 1 + C(A - BK_{lqr})^{-1}B, \quad (69)$$

$$S_I = -\frac{1}{\max \operatorname{Re}\{\lambda_p\}}, \quad (70)$$

$$D_p = \max(|\operatorname{Imag}(\lambda_p)|). \quad (71)$$

The weighted sum scalarization method with equal weights is utilized to solve the multiobjective optimization problem. The performance indices are arranged to produce a single scalar fitness function as given in (67). However, the individual indices have different units; hence, they are normalized to offer a sense of fairness. The normalization is carried out by dividing each objective function by its maximum possible value which can be obtained by running the algorithm for each objective function individually. For such situations, the algorithm provides the minimum value for the required objective at the expense of the others where they could be at their maximums.

For a given wind speed and operating power factor, the linearized system matrices A and B are called from lookup tables stored previously in an offline process. Starting with random values for the elements in the weighting matrices shown in (72) and (73), the Riccati equation is analytically evaluated, and the state feedback gain matrix (K_{LQR}) is determined. The WOA keeps exploring different values for the weighting matrices until finally reporting the optimal solution. The WOA is set to 10 search agents and a maximum number of iterations of 500.

$$\mathbf{Q}_{lqr} = \operatorname{diagonal}([q_1 q_2 q_3 q_4 q_5 q_6]), \quad (72)$$

$$\mathbf{R}_{lqr} = \operatorname{diagonal}([r_1 r_2 r_3 r_4]). \quad (73)$$

6. Grid Support for Real and Reactive Power

Increasing the penetration levels from renewable energy requires newly installed technologies to be more involved in grid reliability aspects during normal operating conditions and following contingencies. Ancillary services involve active power manipulation enabling frequency regulation. On the other hand, reactive power control at the point of common coupling facilitates voltage regulation. In some cases, because of congestion or inertia-related issues, wind farms are forced to curtail or spill the available power. In this context, this section is intended to evaluate the reactive power support capability and the real power curtailments for wind turbines based DFIG.

6.1. Reactive Power Limits. The capability of DFIG providing reactive power support is constrained by several limits. Rated currents for both the stator and the rotor should be respected in any mode of operation. Moreover, the operating limits of the grid-side converter (GSC) while providing reactive power should not be violated [40].

The steady-state model in the $(d-q)$ reference frame can be used to evaluate the reactive power limits while operating in the MPPT region. As previously inferred, the stator's real power is proportional to the rotor quadrature current (i_{qr}). However, the stator's reactive power is linked

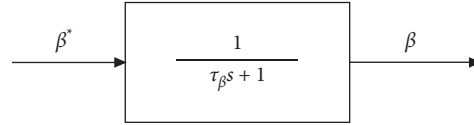


FIGURE 6: Simplified block diagram of pitch control system.

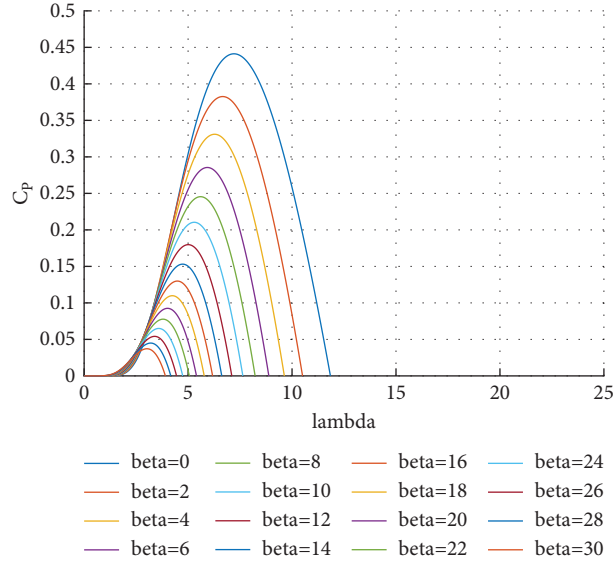


FIGURE 7: Relationship between power coefficient and tip speed ratio at different pitch angles (fixed wind speed of 8 m/s).

TABLE 1: System parameters and equilibrium point at 8 m/s [4, 41].

Par	Value	Par	Value
f	50 Hz	P_s	2 MW
V_s	690 V	R_s	0.0026 Ω
R_r	0.0029 Ω	$L_{ls,r}$	0.087 mH
L_m	2.5 mH	p	4
I_s	1760 A	τ_β	1 s
β_{opt}	0°	λ_{opt}	7.2
J	127 kg.m ²	V_{dc}	1150 V
C_{dc}	80 mF	R	42 m
C_p	0.44	K_{opt}	0.29645
L_f	0.4 mH	R_f	20 $\mu\Omega$
ρ	1.225 kg/m ³	N	100
I_r	1823 A	V_r	488 V
$i_{dr o}$	717.32105 A	i_{qro}	1072.471 A
i_{dgo}	140.1118 A	i_{qgo}	0 A
ω_{rmo}	137.1428 rad/s	$v_{dc o}$	1150 V
$v_{dr o}$	-5.2354 V	v_{qro}	77.1038 V
v_{dfo}	563.3854 V	v_{qfo}	17.6069 V
v_i	3.8 m/s	v_R	12.5 m/s
v_o	15 m/s	P_R	2.4 MW

with the rotor direct current component (i_{dr}). In this context, (i_{qr}) is determined to achieve the MPPT and cannot be altered. Extracting (i_{qr}) from equation (48) at steady state provides an analytical expression for (i_{qr}) at any given wind

speed as shown in (74). Afterward, the maximum rotor current component (i_{dr}) can be evaluated. Finally, stator's reactive power boundaries are calculated by substituting (i_{dr-max}) in (56).

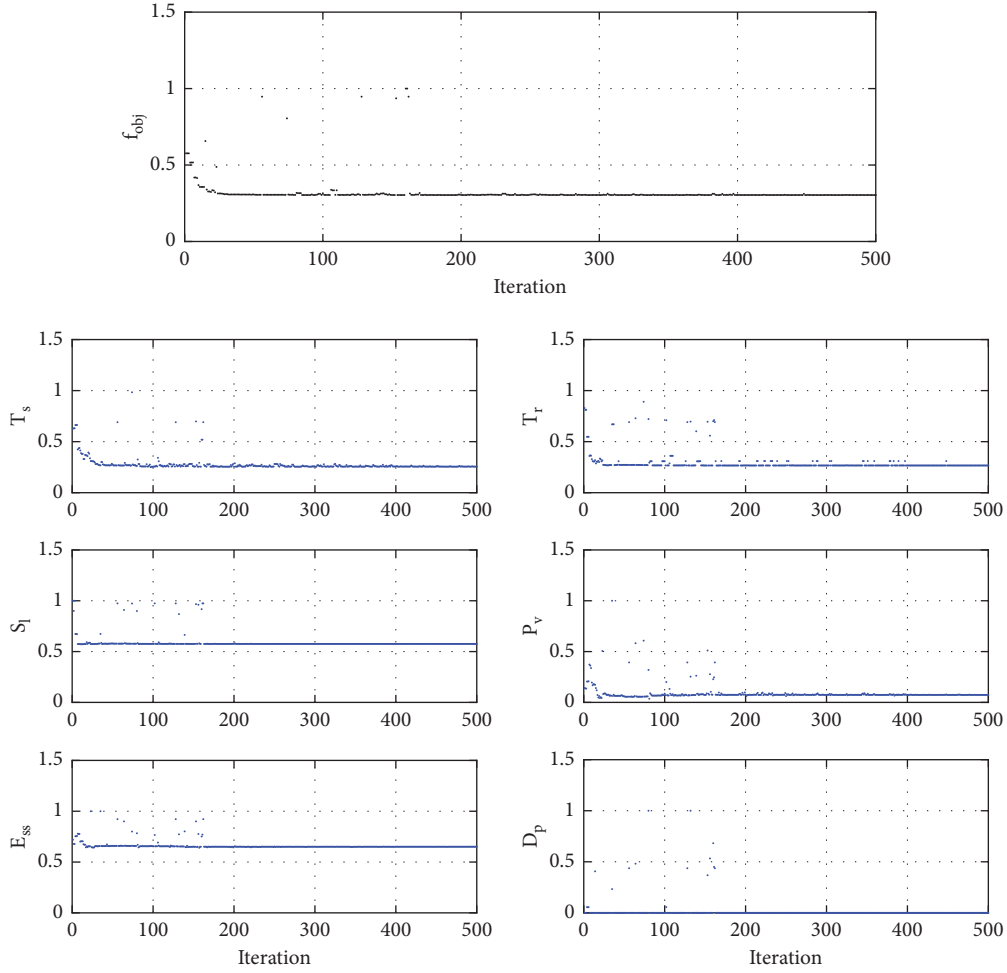


FIGURE 8: Convergence diagram for the objective function and individual indices at wind speed of 8 m/s.

TABLE 2: PI and optimal parameters of LQR.

k_{p1}	k_{i1}	$k_{p2} = k_{p3}$	$k_{i2} = k_{i3}$
0.05	21	0.5771	491.5995
k_{p4}	k_{i4}	$k_{p5} = k_{p6}$	$k_{i5} = k_{i6}$
-1000	-300000	0.2513	39.4784
Q_1	Q_2	Q_3	Q_4
20.6737	41.6646	19.3643	28.201
Q_5	Q_6	R_1	R_2
9.2443	76.9038	11.9002	32.9333
R_3	R_4	—	—
11.121	76.9038	—	—

$$i_{qr} = \frac{4K_{opt}w_{rm}^2L_s}{3P\Psi_{ds}L_m}, \quad (74)$$

$$i_{dr-\max} = \pm \sqrt{I_{r-\text{rated}}^2 - i_{qr}^2}, \quad (75)$$

$$w_{rm} = \frac{\lambda_{opt}v_w N}{R}, \quad (76)$$

current limit. After evaluating (i_{qr}) at a particular wind speed, the stator quadrature current component (i_{qs}) is determined as shown in (77). Accordingly, the maximum stator d – axis component can be found. Therefore, stator reactive power limited by stator current is calculated using equation (38).

$$i_{qs} = -\frac{L_m}{L_s}i_{qr}, \quad (77)$$

$$i_{ds-\max} = \pm \sqrt{I_{s-\text{rated}}^2 - i_{qs}^2}, \quad (78)$$

and, on the other hand, reactive power support could be constrained by the stator current limit rather than the rotor

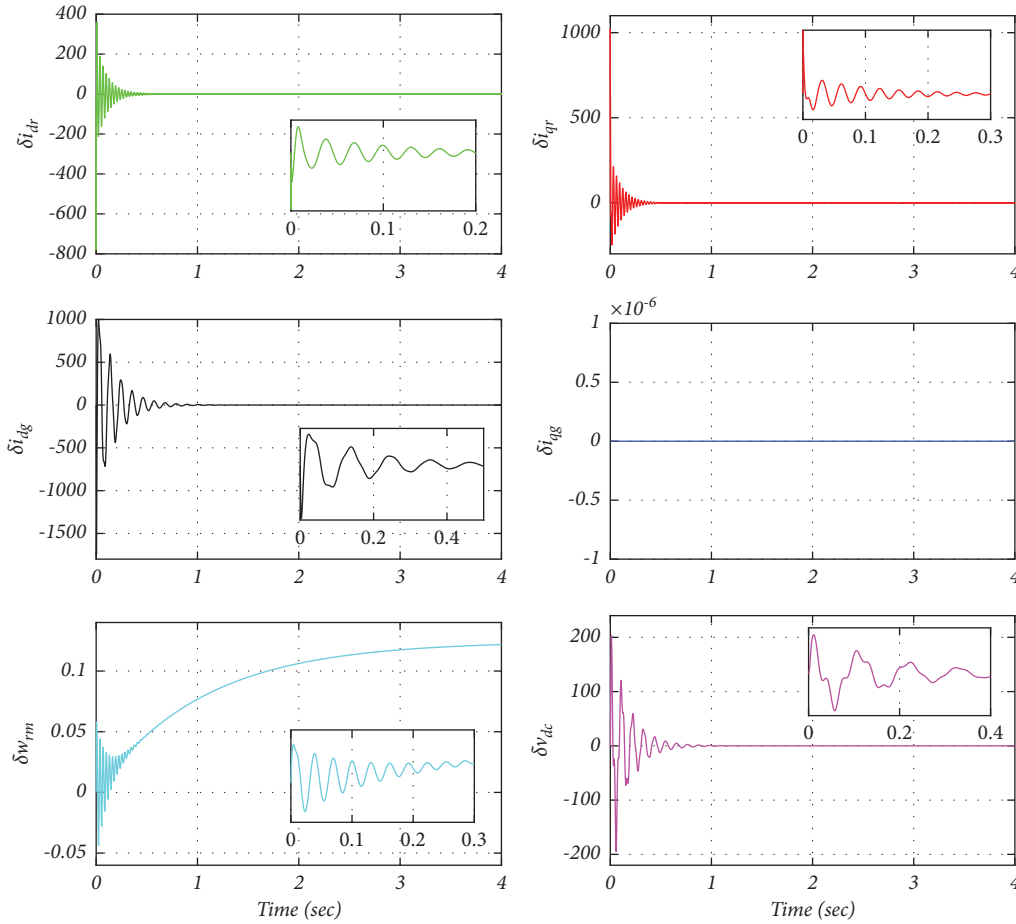


FIGURE 9: Response of state variables deviations with PI regulator at fixed wind speed of 8 m/s.

Two different boundaries resulted from the limits of rotor and stator currents. However, the actual reactive power capability is determined by which the boundaries are reached first. Further, operating at the MPPT limits the amount of reactive power which could be absorbed or delivered. Therefore, reactive power support can be improved by allowing active power curtailments.

6.2. Real Power Curtailment. Wind turbines can also participate in active power ancillary services such as frequency regulation and spinning reserves. For such cases, the operation is not following MPPT. Instead, partial curtailment is performed to give a real power margin available for emergencies. Furthermore, active power curtailment improves the reactive power capability of the machine. Curtailment is performed by activating the pitch control mechanism even at the MPPT region. A pitch actuator is a mechanical system that represents the dynamic behavior between the required and measured pitch angles. Figure 6 shows a block diagram of a pitch control system actuated by a servomotor represented by

a first-order model. Based on the approximated nonlinear dynamics of pitch control system [44], the time derivative of pitch angle can be described by (79). This equation is added to represent the state-space model where a new state variable (β) and input (β^*) are included.

$$\frac{d\beta}{dt} = \frac{1}{\tau_\beta} (\beta^* - \beta). \quad (79)$$

Wind turbines operating at Maximum Power Point should work at the optimum pitch angle and tip speed ratio. For power reductions, pitch angle increases proportional to the power content in the mainstream wind. This is performed to extract only the required active power. At any particular wind speed, the required output power is defined, where its upper limit is the maximum power extracted at maximum efficiency. This determines the power coefficient (C_p) which achieves the power reduction as previously shown in equation (1). For illustration, Figure 7 shows the relation between (C_p) and (λ) at different pitch angle (β).

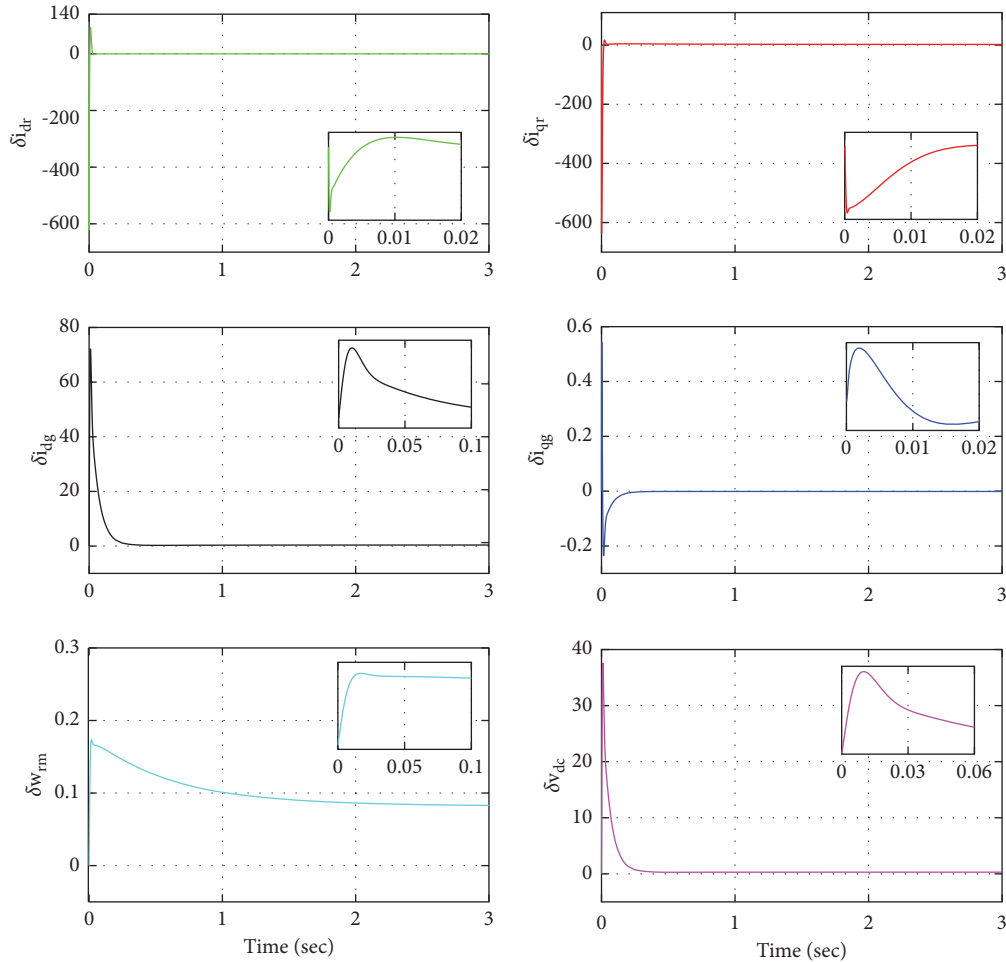


FIGURE 10: Response of state variables with optimized LQR regulator at fixed wind speed of 8 m/s.

From these curves, it is required to select (β) and (λ) which provide the expected (C_p) that limits the turbine mechanical power.

7. Simulation Results

To evaluate the performance of the proposed LQR controller, a 2.4 MW wind turbine is used in our simulation. The machine parameters are as listed in Table 1. From simulation, state variables (δi_{dr} , δi_{qr} , δi_{dg} , δi_{qg} , δw_{rm} , δv_{dc}) and real and reactive power of stator and rotor are obtained.

The WOA initially uses random values for the elements in the weighting matrices (Q_{lqr} and R_{lqr}). Then, the algorithm explores alternatives until final convergence and reports the optimal values found. A convergence diagram is provided in Figure 8 for the objective function and the individual indices at wind speed of 8 m/s. Controllers design parameters for both the PI and the LQR are listed in Table 2.

The time-domain responses for all state variables for the conventional PI controller and the proposed LQR controller are demonstrated in Figures 9 and 10, respectively. The

simulation is conducted at a fixed wind speed of 8 m/s and unity power factor. Initial values are selected as the equilibrium point of the linearized system as previously described in Algorithm 1. Numerical values of all initial conditions are provided in Table 1. It can be noticed that the proposed controller provides smaller peak value, settling time, and oscillation. In this context, the optimized LQR can stabilize the system more efficiently compared to the PI controller.

To demonstrate the effectiveness of the proposed controller, a wind speed variation is considered as shown in the top-left graph of Figure 11. The linear system matrices and the optimal feedback gain matrix are adjusted as the wind speed changes at a very fine discrete wind speed domain. Wind velocity changes as a sine wave covering the entire MPPT region, that is, both the subsynchronous and hypersynchronous regions. The figure compares the performances of the PI controller, conventional LQR, and the gain-scheduling LQR. The top-right graph shows the total active power extracted from the turbine. The middle plots show stator and rotor active power, while the bottom graphs

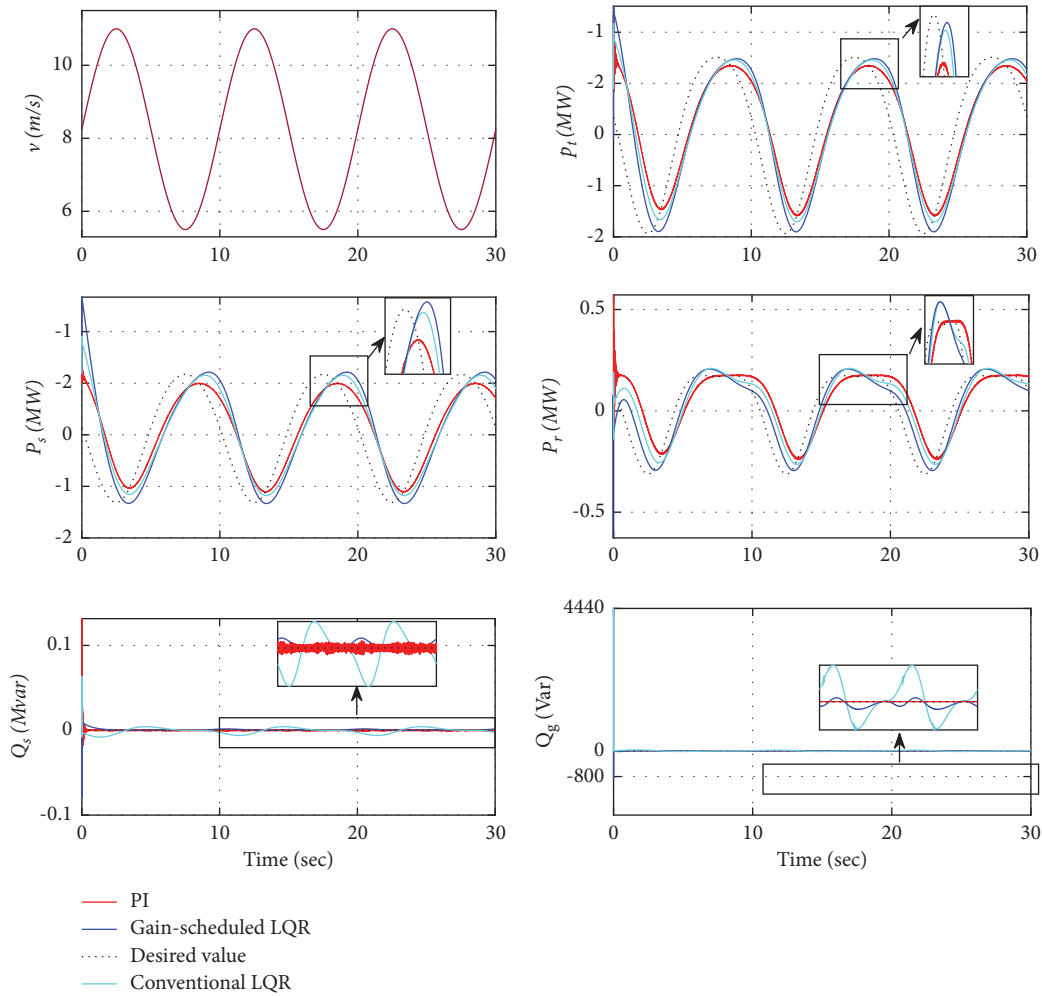


FIGURE 11: Output real/reactive power with PI, conventional LQR, and gain-scheduling LQR at different wind speed.

illustrate the stator and rotor reactive power. It is clearly seen that the proposed controller follows the expected theoretical value at a faster rate and it is even closer to the maximum expected value. From energy production perspectives, this marginal power enhancement will have a great improvement, especially in regions experiencing high wind speed variations.

Finally, a simulation for reactive power capability at the region of MPPT is provided. Figure 12 illustrates the reactive power boundaries (middle-right graph) as wind speed increases from 5.5 to 11 m/s. In this simulation, the maximum power extracting capability is achieved at the optimum pitch angle. It is clearly shown that as the output real power increases, the reactive power support boundaries decrease to smaller margins. In the lagging mode of operation, the rated rotor current determines the maximum reactive power which can be provided to the network. However, in the leading mode, the stator current governs the reactive power

which can be absorbed. On the other hand, in Figure 13, pitch angle control is activated to curtail output power at the minimum value (212 kW). As shown in the middle-right graph, this action maintains the maximum reactive power support capability over the entire region.

7.1. Current Limitations and Future Work

- (1) The work presented in the paper is verified only using simulation. Our future work orientation is to validate the proposed methodology experimentally.
- (2) Design changes are required to achieve robustness against parameter variation and disturbance rejection.
- (3) Evaluate the controller performance with appropriate design changes under both voltage and frequency transients at the grid side.

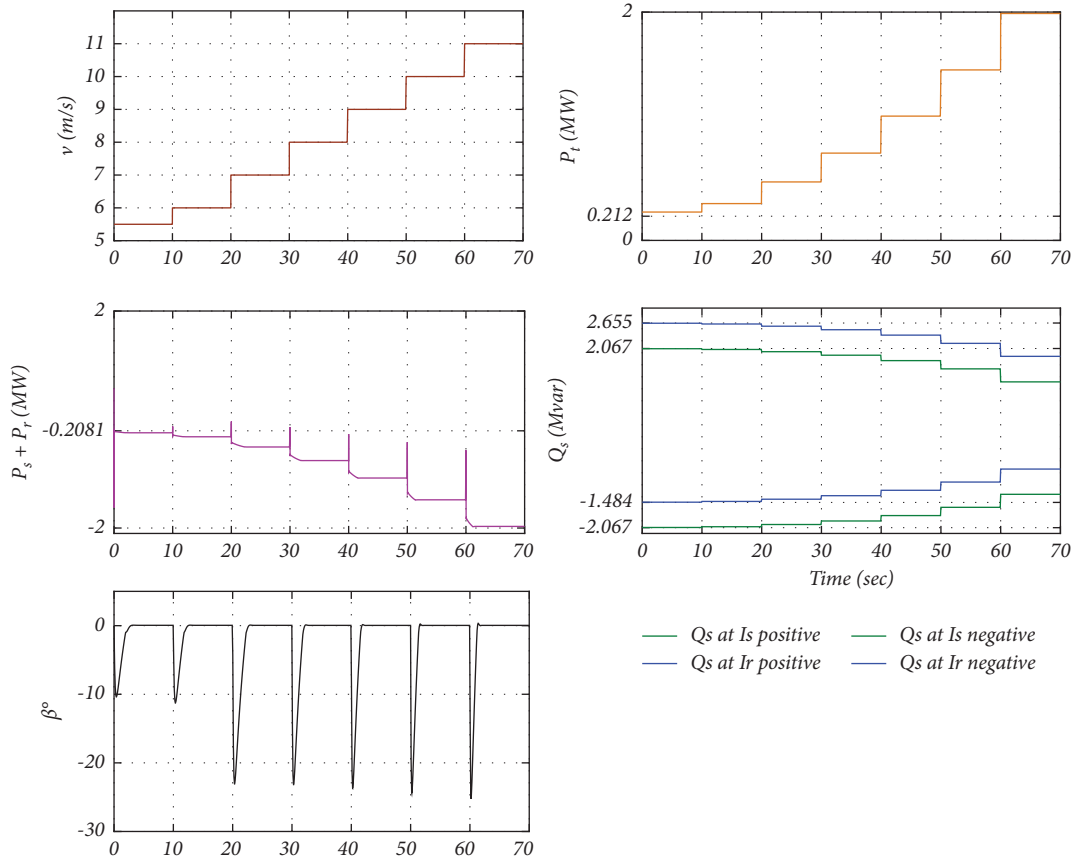


FIGURE 12: Reactive power capability of DFIG operating at MPPT.

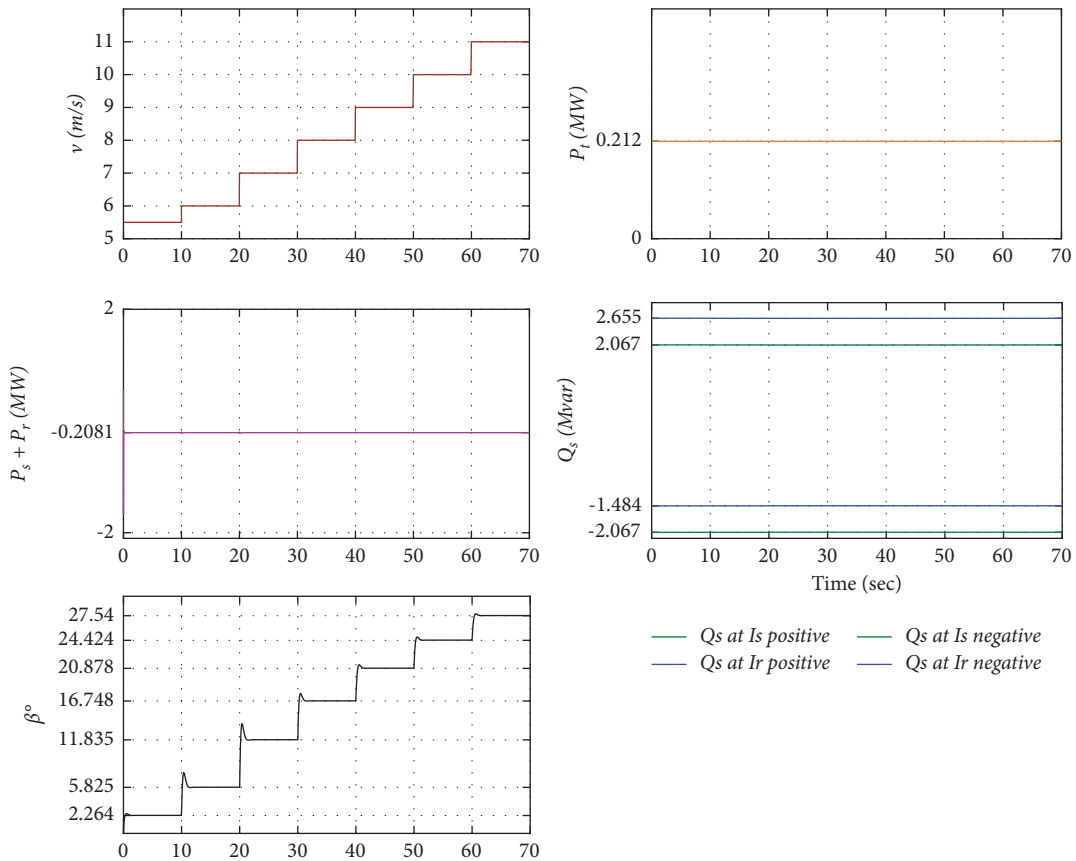


FIGURE 13: Reactive power capability of DFIG with real power curtailment.

8. Conclusion

This paper proposes linear quadratic regulator (LQR) with optimal gain-scheduling for wind turbines based on Doubly Fed Induction Generators. The whale optimization technique is used in this study to find the optimal weighting matrices that guarantee the optimal performance at any particular wind speed. The process is repeated offline at a discrete wind speed domain. The corresponding results are stored in lookup tables to be used during the online implementation. Based on the profile of wind speed variation, the controller parameters are updated from the lookup tables. Compared with the conventional PI controller, the results have shown that the performance of the proposed LQR controller is stable, it has faster responses, and it is able to extract the maximum theoretical power more precisely. Moreover, the proposed controller preserves linearity and simplicity and is presented in a more compact form.

In addition, the effect of pitch angle control is augmented to the controller for real power curtailment capability. This enables wind turbines to support the grid and participate in various real power ancillary services. Furthermore, the effects of real power reductions on enhancing the reactive power supporting capability are demonstrated.

Nomenclature

β :	Pitch angle
λ :	Tip speed ratio
A :	State matrix
B :	Input matrix
C :	Output matrix
D :	Feed-through matrix
u :	Input variables vector
y :	Output variables vector
Ω_t :	Turbine rotor angular speed
$\psi_{ds}, \psi_{qs}, \psi_{dr}, \psi_{qr}$:	Stator/rotor flux linkages
ρ :	Air density (kg/m ³)
σ :	Leakage coefficient
τ_β :	Pitch control time constant
τ_r, τ_g :	Time constants of PI current control
ζ :	Damping ratio
A_t :	Surface area (m ²)
C_p :	Power coefficient
C_t :	Torque coefficient
C_{bus} :	DC link capacitance
D_t, D_m :	Damping coefficients
E_{ss} :	Steady-state error
f_{obj} :	Objective function
$i_{ds}, i_{qs}, i_{dr}, i_{qr}$:	Stator and rotor d - q currents
$I_{r-rated}$:	Rated rotor current
$I_{s-rated}$:	Rated stator current
J :	Moment of inertia
J_{LQR} :	Quadratic cost function
L_f :	Grid-side filter inductance
L_m :	Mutual inductance
L_r :	Rotor self-inductance
L_s :	Stator self-inductance
$L_{\sigma r}$:	Rotor winding leakage inductance

$L_{\sigma s}$:	Stator winding leakage inductance
N :	Gearbox ratio
p :	Number of poles
P_g, Q_g :	Grid real and reactive power
P_R :	Turbine rated power
P_s, Q_s, P_r, Q_r :	Stator/rotor real and reactive power
$P_w(v)$:	Wind kinetic energy
P_{dc} :	DC link power
P_{lqr} :	Riccati equation solution matrix
P_v :	Peak value
Q_{lqr} :	Diagonal semipositive definite matrix
R :	Radius of wind turbine rotor (m)
R_f :	Grid-side filter resistance
R_s, R_r :	Stator and rotor resistances
R_{lqr} :	Diagonal positive definite matrix
S_I :	Stability index
T_{em} :	Electromagnetic torque
T_{mech} :	Turbine mechanical torque
T_r :	Rising time
T_s :	Settling time
v :	Wind speed (m/s)
v_i :	Cut-in wind speed
v_o :	Cut-out wind speed
v_R :	Rated wind speed
v_{dc}, i_{dc} :	DC link voltage and current
$v_{df}, v_{qf}, i_{dg}, i_{qg}$:	GSC d - q voltages/currents
v_{dg}, v_{qg} :	Grid d - q voltages
$v_{ds}, v_{qs}, v_{dr}, v_{qr}$:	Stator and rotor d - q voltages
ω_r :	Rotor frequency-electrical (rad/sec)
ω_s :	Synchronous frequency-electrical (rad/sec)
ω_{nr}, ω_{ng} :	Natural frequencies of PI current control
ω_{re} :	Rotor electrical speed (rad/sec)
ω_{rm} :	Rotor mechanical speed.

Data Availability

The data are available upon request from the corresponding author (Dr. Ashraf Radaideh; e-mail: a.radaideh@yu.edu.jo; alternative e-mail: ashraf.radaideh86@gmail.com; Tel: +962 2 7211111 EX1-Dep. 4239. EX2-office 4305).

Conflicts of Interest

The authors declare that they have no conflicts of interest.

References

- [1] Global Wind Energy Council, *GWEC Global Wind Report 2021*, WindEnergy Hamburg Press Releases, Hamburg, Germany, 2021.
- [2] L. Zhang and W. Shepherd, *Electricity Generation Using Wind Power. [Hackensack]*, World Scientific, New Jersey, NJ, USA, 2017.
- [3] H. A.-R. Kamal Al-Haddad and M. Malinowski, *Power Electronics for Renewable Energy Systems, Transportation and Industrial Applications*, John Wiley & Sons, Hoboken, NJ, USA, 2014.
- [4] G. Abad, J. Lopez, M. Rodriguez, L. Marroyo, and G. Iwanski, *Doubly Fed Induction Machine: Modeling and Control for*

- Wind Energy Generation*, Vol. 85, John Wiley & Sons, Hoboken, NJ, USA, 2011.
- [5] S. L. S. Domingos, E. A. A. Arthur, and F. D. C. Oliveira, "Chapter 15-doubly fed induction generator in wind energy conversion systems," in *Advances in Renewable Energies and Power Technologies*, I. Yahyaoui, Ed., vol. 1, pp. 461–490, Elsevier, Amsterdam, Netherlands, 2018.
 - [6] A. Gundavarapu, H. Misra, and K. J. Amit, "Direct torque control scheme for DC voltage regulation of the standalone DFIG-DC system," *IEEE Transactions on Industrial Electronics*, vol. 64, no. 5, pp. 3502–3512, 2016.
 - [7] Z. Boudjema, R. Taleb, Y. Djeriri, and Y. Adil, "A novel direct torque control using second order continuous sliding mode of a doubly fed induction generator for a wind energy conversion system," *Turkish Journal of Electrical Engineering and Computer Sciences*, vol. 25, no. 2, pp. 965–975, 2017.
 - [8] A. Nazari and H. Heydari, "Direct power control topologies for DFIG-based wind plants," *International Journal of Computer and Electrical Engineering*, vol. 4, no. 4, Article ID 475, 2012.
 - [9] M. K. Bourdoulis and T. A. Antonio, "Direct power control of DFIG wind systems based on nonlinear modeling and analysis," *IEEE journal of emerging and selected topics in power electronics*, vol. 2, no. 4, pp. 764–775, 2014.
 - [10] L. Xiong, J. Wang, M. Xiao, and M. W. Khan, "Fractional order sliding mode based direct power control of grid-connected DFIG," *IEEE Transactions on Power Systems*, vol. 33, no. 3, pp. 3087–3096, 2017.
 - [11] L. Djilali, E. N. Sanchez, and M. Belkheiri, "Real-time implementation of sliding-mode field-oriented control for a DFIG-based wind turbine," *International Transactions on Electrical Energy Systems*, vol. 28, no. 5, Article ID e2539, 2018.
 - [12] B. Subudhi and S. O. Pedda, "Optimal preview stator voltage-oriented control of DFIG WECS," *IET Generation, Transmission & Distribution*, vol. 12, no. 4, pp. 1004–1013, 2017.
 - [13] E. E. Özsoy, E. Golubovic, A. Sabanovic, S. Bogosyan, and G. Metin, "Modeling and control of a doubly fed induction generator with a disturbance observer: a stator voltage oriented approach," *Turkish Journal of Electrical Engineering and Computer Sciences*, vol. 24, no. 3, pp. 961–972, 2016.
 - [14] S. Karad and R. Thakur, "Recent trends of control strategies for doubly fed induction generator based wind turbine systems: a comparative review," *Archives of Computational Methods in Engineering*, vol. 28, pp. 15–29, 2019.
 - [15] H.-S. Ko, G.-G. Yoon, N.-H. Kyung, and W.-P. Hong, "Modeling and control of DFIG-based variable-speed wind-turbine," *Electric Power Systems Research*, vol. 78, no. 11, pp. 1841–1849, 2008.
 - [16] R. Pena, J. C. Clare, and G. M. Asher, "Doubly fed induction generator using back-to-back PWM converters and its application to variable-speed wind-energy generation," *IEE Proceedings - Electric Power Applications*, vol. 143, no. 3, pp. 231–241, 1996.
 - [17] G.-S. Byeon, I.-K. Park, and G. Jang, "Modeling and control of a doubly-fed induction generator (DFIG) wind power generation system for real-time simulations," *Journal of Electrical Engineering and Technology*, vol. 5, pp. 61–69, 2010.
 - [18] B. Yang, L. Jiang, L. Wang, W. Yao, and Q. H. Wu, "Nonlinear maximum power point tracking control and modal analysis of DFIG based wind turbine," *International Journal of Electrical Power & Energy Systems*, vol. 74, pp. 429–436, 2016.
 - [19] G. S. Kaloi, J. Wang, and M. Hussain Baloch, "Active and reactive power control of the doubly fed induction generator based on wind energy conversion system," *Energy Report*, vol. 2, pp. 194–200, 2016.
 - [20] R. Cardenas, R. Pena, J. Proboste, G. Asher, and J. Clare, "MRAS observer for sensorless control of standalone doubly fed induction generators," *IEEE Transactions on Energy Conversion*, vol. 20, no. 4, pp. 710–718, 2005.
 - [21] C. Cheng, P. Cheng, H. Nian, and D. Sun, "Model predictive stator current control of doubly fed induction generator during network unbalance," *IET Power Electronics*, vol. 11, no. 8, 2017.
 - [22] K. Qingmei, W. Xiangdong, and L. Shujiang, "A novel sliding mode control of doubly-fed induction generator for optimal power extraction," in *Proceedings of the 2019 IEEE Innovative Smart Grid Technologies-Asia (ISGT Asia)*, pp. 1318–1323, Chengdu, China, May 2019.
 - [23] F. Fateh, W. N. White, and D. Gruenbacher, "A maximum power tracking technique for grid-connected DFIG-based wind turbines," *IEEE Journal of Emerging and Selected Topics in Power Electronics*, vol. 3, no. 4, pp. 957–966, 2015.
 - [24] M. Krstic, *Delay Compensation for Nonlinear, Adaptive, and Pde Systems*, Birkhäuser, Basel, Switzerland, 2009.
 - [25] J. Ritonja, "Adaptive stabilization for generator excitation system," *COMPEL-The International Journal for Computation and Mathematics in Electrical and Electronic Engineering*, vol. 30, no. 3, 2011.
 - [26] D. G. Forchetti, G. O. Garcia, and I. V. Maria, "Adaptive observer for sensorless control of stand-alone doubly fed induction generator," *IEEE Transactions on Industrial Electronics*, vol. 56, no. 10, pp. 4174–4180, 2009.
 - [27] S. Yang and V. Ajarapu, "A speed-adaptive reduced-order observer for sensorless vector control of doubly fed induction generator-based variable-speed wind turbines," *IEEE Transactions on Energy Conversion*, vol. 25, no. 3, pp. 891–900, 2010.
 - [28] R. Syahputra, I. Robandi, and M. Ashari, "Control of doubly-fed induction generator in distributed generation units using adaptive neuro-fuzzy approach," in *Proceedings of the International Seminar on Applied Technology, Science and Arts (APTECS)*, pp. 493–501, Surabaya, Indonesia, December 2011.
 - [29] D.-C. Phan and S. Yamamoto, "Rotor speed control of doubly fed induction generator wind turbines using adaptive maximum power point tracking," *Energy*, vol. 111, pp. 377–388, 2016.
 - [30] C. A. Evangelista, A. Pisano, P. Paul, and E. Usai, "Receding horizon adaptive second-order sliding mode control for doubly-fed induction generator based wind turbine," *IEEE Transactions on Control Systems Technology*, vol. 25, no. 1, pp. 73–84, 2016.
 - [31] N. Ullah, M. Asghar Ali, A. Ibeas, and J. Herrera, "Adaptive fractional order terminal sliding mode control of a doubly fed induction generator-based wind energy system," *IEEE Access*, vol. 5, pp. 21368–21381, 2017.
 - [32] F. Mazouz, S. Belkacem, I. Colak, S. Drid, and Y. Harbouche, "Adaptive direct power control for double fed induction generator used in wind turbine," *International Journal of Electrical Power & Energy Systems*, vol. 114, Article ID 105395, 2020.
 - [33] B. Yang, X. Zhang, T. Yu, H. Shu, and Z. Fang, "Grouped grey wolf optimizer for maximum power point tracking of doubly-fed induction generator based wind turbine," *Energy Conversion and Management*, vol. 133, pp. 427–443, 2017.
 - [34] S. Abdeddaim and A. Betka, "Optimal tracking and robust power control of the DFIG wind turbine," *International Journal of Electrical Power & Energy Systems*, vol. 49, pp. 234–242, 2013.

- [35] K. Bedoud, M. Ali-rachedi, T. Bahi, R. Lakel, and A. Grid, "Robust control of doubly fed induction generator for wind turbine under sub-synchronous operation mode," *Energy Procedia*, vol. 74, pp. 886–899, 2015.
- [36] S. Alepuz, S. Busquets-Monge, J. Bordonau, J. Gago, D. Gonzalez, and J. Balcells, "Interfacing renewable energy sources to the utility grid using a three-level inverter," *IEEE Transactions on Industrial Electronics*, vol. 53, no. 5, pp. 1504–1511, 2006.
- [37] R. H. Dorf and R. C. Bishop, *Modern Control Systems*, Pearson College Div (US), Hudson, NY, USA, 2016.
- [38] R. Rocha, A. C. Gilmar, J. F. Alexandre, and F. Allison Torga, "Multivariable H_2 and H_∞ control for a wind energy conversion system: a comparison," *Journal of the Brazilian Society of Mechanical Sciences and Engineering*, vol. 32, no. 4, pp. 510–518, 2010.
- [39] R. Bhushan and K. Chatterjee, "Mathematical modeling and control of DFIG-based wind energy system by using optimized linear quadratic regulator weight matrices," *International Transactions on Electrical Energy Systems*, vol. 27, no. 9, pp. 1–23, 2017.
- [40] S. Engelhardt, Istvan Erlich, C. Feltes, J. Kretschmann, and F. Shewarega, "Reactive power capability of wind turbines based on doubly fed induction generators," *IEEE Transactions on Energy Conversion*, vol. 26, no. 1, pp. 364–372, 2010.
- [41] D. Xie, Z. Xu, L. Yang, Ø. Jacob, Y. Xue, and K. P. Wong, "A comprehensive LVRT control strategy for DFIG wind turbines with enhanced reactive power support," *IEEE Transactions on Power Systems*, vol. 28, no. 3, pp. 3302–3310, 2013.
- [42] M. S. Raluca, C. L. Prioroc, and A. M. Stoica, "Weighting matrices determination using pole placement for tracking maneuvers," *UPB Scientific Bulletin, Series D*, vol. 75, no. 2, pp. 31–41, 2013.
- [43] S. Mirjalili and A. Lewis, "The whale optimization algorithm," *Advances in Engineering Software*, vol. 95, pp. 51–67, 2016.
- [44] M. H. Christoph, P. Jané-Soneira, M. Pfeifer, K. Schechner, and S. Hohmann, "Full-and reduced-order state-space modeling of wind turbine systems with permanent magnet synchronous generator," *Energies*, vol. 11, no. 7, Article ID 1809, 2018.